

Far-field constant-gradient laser accelerator of electrons in an ion channel

Vladimir N. Khudik, Xi Zhang, Tianhong Wang, and Gennady Shvets

Citation: *Physics of Plasmas* **25**, 083101 (2018); doi: 10.1063/1.5036967

View online: <https://doi.org/10.1063/1.5036967>

View Table of Contents: <http://aip.scitation.org/toc/php/25/8>

Published by the *American Institute of Physics*

Articles you may be interested in

[High-charge energetic electron bunch generated by multiple intersecting lasers](#)

Physics of Plasmas **25**, 083102 (2018); 10.1063/1.5037755

[Generation of keV hot near-solid density plasma states at high contrast laser-matter interaction](#)

Physics of Plasmas **25**, 083103 (2018); 10.1063/1.5027463

[Collective “overacceleration” of electrons in a pinched picosecond electron beam](#)

Physics of Plasmas **25**, 083106 (2018); 10.1063/1.5033364

[Towards realistic simulations of QED cascades: Non-ideal laser and electron seeding effects](#)

Physics of Plasmas **25**, 083104 (2018); 10.1063/1.5022640

[Electron shock-surfing acceleration in the presence of magnetic field](#)

Physics of Plasmas **25**, 082103 (2018); 10.1063/1.5030184

[Computational modeling of proton acceleration with multi-picosecond and high energy, kilojoule, lasers](#)

Physics of Plasmas **25**, 083109 (2018); 10.1063/1.5040410



ULVAC

Leading the World with Vacuum Technology

- Vacuum Pumps
- Arc Plasma Deposition
- RGAs
- Leak Detectors
- Thermal Analysis
- Ellipsometers

Far-field constant-gradient laser accelerator of electrons in an ion channel

Vladimir N. Khudik,^{1,2} Xi Zhang,¹ Tianhong Wang,² and Gennady Shvets²

¹Department of Physics and Institute for Fusion Studies, The University of Texas at Austin, Austin, Texas 78712, USA

²School of Applied and Engineering Physics, Cornell University, Ithaca, New York 14850, USA

(Received 19 April 2018; accepted 13 July 2018; published online 30 July 2018)

We predict that electrons in an ion channel can gain ultra-relativistic energies by simultaneously interacting with a laser pulse and, counter-intuitively, with a decelerating electric field. The crucial role of the decelerating field is to maintain high-amplitude betatron oscillations, thereby enabling constant rate energy flow to the electrons via the inverse ion channel laser mechanism. Multiple harmonics of the betatron motion can be employed. Injecting electrons into a decelerating phase of a laser wakefield accelerator is one practical implementation of the scheme. *Published by AIP Publishing.*

<https://doi.org/10.1063/1.5036967>

I. INTRODUCTION

Far-field accelerators occupy an important niche in the field of advanced electron accelerators. Such accelerators utilize a transverse electromagnetic wave that resonantly interacts with electrons undergoing transverse motion. Examples of such transverse motion include electron undulation in the transverse magnetic field, electron gyration in the longitudinal magnetic field, or betatron motion in the confining focusing channel. The corresponding accelerator schemes are, respectively, referred to as inverse free-electron laser FEL,^{1–3} cyclotron resonance laser (CRL),^{4–6} and ion-channel laser (ICL).^{7–9}

The main advantage of the far-field inverse laser schemes is their simplicity: no electromagnetic structure is required because the acceleration is accomplished by the $W_{\parallel} \propto \vec{v}_{\perp} \times \vec{B}_{\perp}^{(L)}$ force directly exerted on the electron beam by the transverse component of the laser's electromagnetic fields $(\vec{E}^{(L)}, \vec{B}^{(L)})$. The main drawback is that, in general, the acceleration gradient W_{\parallel} tends to decrease as the relativistic electron energy γmc^2 increases. For example, $W_{\parallel} \propto 1/\gamma$ for inverse FELs and $W_{\parallel} \propto 1/\sqrt{\gamma}^5$ for inverse CRLs, thereby reducing the usefulness of these schemes to moderate γ 's. Such reduction is caused by a rapid decrease in $|\vec{v}_{\perp}|$ and cannot be cured by simply maintaining the wave-particle synchronism.^{5,6} Therefore, it can only be overcome if a suitable mechanism for steadily increasing the magnitude of the transverse electron momentum $\vec{p}_{\perp} = \gamma m \vec{v}_{\perp}$, as well as its phase with respect to the laser field $\vec{E}^{(L)}$, can be found.

In this paper, we propose that both requirements can be satisfied for an inverse ICL if a small constant *decelerating* longitudinal electric field is applied to the electrons undergoing betatron motion inside an ion channel. The channel can be produced by the space charge of the electron beam itself,^{7,10} or by the ponderomotive pressure of an ultra-intense laser pulse that creates a plasma “bubble.”¹¹ Practical realization of the inverse ICL, where electrons are externally injected into the leading (decelerating) part of the plasma bubble, is suggested and analyzed using particle-in-cell (PIC) simulations.

The relativistic electron dynamics is analytically reduced to that of a nonlinear pendulum.

Earlier work on direct laser acceleration (DLA)^{8,9,12–15} demonstrated that a relatively small energy from the laser, ΔA_L , can be added to that gained from the *accelerating* longitudinal electric field, $\Delta A_W > 0$, under special electron injection conditions and laser pulse formats: large initial transverse energy of the injected electrons and the elongated, asymmetric, or multi-peaked laser pulse.^{13–15} The unique feature of the acceleration mechanism proposed in this paper is that the small longitudinal electric field actually *reduces* the energy of the beam by $\Delta A_W < 0$, but in doing so modifies the transverse electron dynamics to ensure that the direct energy gain is twice as high: $\Delta A_L \approx 2|\Delta A_W|$. Moreover, the above stringent conditions on the laser and the electron beam need not apply.

The rest of the paper is organized as follows: In Sec. II, we introduce a minimal model of the electron acceleration in an ion channel under the combined action of the oscillating laser field and the stationary longitudinal decelerating electric field. We qualitatively analyze and numerically solve the relativistic equations of electron motion. In Sec. III, we develop an analytical theory drawing analogy with the motion of a pendulum and explain the essential features of electron acceleration in the presence of a longitudinal decelerating field. Section IV presents PIC simulations validating the developed theory. Conclusions and future research directions are summarized in Sec. V.

II. MINIMAL MODEL AND QUALITATIVE ANALYSIS

We start by introducing a simple model of the electron motion in the combined focusing field $\vec{F}_{\perp} = -m\omega_p^2 \vec{r}_{\perp}/2$ of a cylindrical ion channel (where $\omega_p = \sqrt{4\pi e^2 n/m}$ is the plasma frequency, n is the plasma density, m is the electron mass, and $\vec{r}_{\perp} = y\vec{e}_y + z\vec{e}_z$ is the transverse electron's position), the electromagnetic field of a linearly (y -)polarized laser beam propagating with the phase velocity v_{ph} in the x -direction, and a constant decelerating electric field $\vec{E}_{dec} = \vec{e}_x E_{\parallel}$. The planar laser fields are assumed in the form

of $E_y^{(L)} = E_0 \cos \varphi$ and $B_z^{(L)} = cE_y^{(L)}/v_{ph}$, where $\varphi = \omega_L(x/v_{ph} - t)$ is the laser phase. The relativistic equations of motion are given by

$$\frac{d}{dt} \left(\gamma \frac{dx}{dt} \right) = -\frac{e}{m} \left(E_{\parallel} + E_0 \frac{v_y \cos \varphi}{v_{ph}} \right), \quad (1)$$

$$\frac{d}{dt} \left(\gamma \frac{dy}{dt} \right) = -\frac{\omega_p^2 y}{2} + \frac{eE_0}{m} \left(\frac{v_x}{v_{ph}} - 1 \right) \cos \varphi, \quad (2)$$

where $\dot{x} = v_x = p_x/m\gamma$, $\dot{y} = v_y = p_y/m\gamma$, and $\dot{f} \equiv df/dt$ for any variable f .

An integral of motion I_0 can be derived from Eqs. (1) and (2)

$$I_0 = \gamma - \frac{p_x v_{ph}}{mc^2} + \frac{\omega_p^2 y^2}{4c^2} + \frac{eE_{\parallel} v_{ph}}{\omega_L mc^2} \varphi, \quad (3)$$

and the definition of $\gamma = (1 + p_x^2/m^2c^2 + p_y^2/m^2c^2)^{1/2}$ can be used in combination with Eq. (3) to express p_y in terms of (φ, p_x) , thereby eliminating the transverse dynamics given by Eq. (2). In the paraxial approximation ($p_x^2 \gg p_y^2 \gg m^2c^2$), the transverse energy^{16,17} $\varepsilon_{\perp} = \frac{1}{2c} |p_x| \dot{y}^2 + \frac{1}{4} m\omega_p^2 y^2$ can be conveniently expressed as

$$\varepsilon_{\perp} = mc^2 I_0 - \frac{eE_{\parallel} v_{ph}}{\omega_L} \varphi + v_{ph} p_x - c|p_x|. \quad (4)$$

Equation (4) is greatly simplified in the case of a luminous laser pulse with $v_{ph} = c$. After taking into account that $\dot{\varphi} \propto (v_x/c - 1) < 0$ and assuming that the electrons are accelerated in the forward direction by the laser, i.e., $p_x > 0$, it follows that $\dot{\varepsilon}_{\perp} \propto E_{\parallel}$. This result implies that, regardless of the amplitude of the laser, the *accelerating* longitudinal field ($-eE_{\parallel} > 0$) depletes the energy of transverse oscillations ε_{\perp} , thereby suppressing the inverse ICL mechanism. Therefore, the effective synergy of DLA and longitudinal field acceleration can be achieved only for those electrons with large initial transverse energy,¹⁵ thus constraining the injection.

A very different dynamics, which is the subject of this paper, emerges in the case of the *decelerating* longitudinal field ($-eE_{\parallel} < 0$), where two scenarios can be realized: (1) ε_{\perp} increases for the forward-accelerated electrons and (2) ε_{\perp} decreases for the electrons accelerated in the backward direction ($p_x < 0$) by the longitudinal field. Because the inverse ICL mechanism is suppressed in the latter case, we concentrate on scenario (1), where the longitudinal field pumps energy into transverse betatron oscillations, thereby enabling steady-state acceleration of the particle by the laser wave against the decelerating force $-eE_{\parallel}$.

The effect of the decelerating longitudinal electric field enhancing the energy of the transverse motion is counter-intuitive because, while the two degrees of freedom are decoupled for non-relativistic particles, it is no longer the case for ultra-relativistic electrons. Specifically, by rewriting Eq. (2) without the laser field in a more conventional form^{12,18} as $\ddot{y} + \Gamma \dot{y} + \omega_{\beta}^2 y = 0$, where $\omega_{\beta} = \omega_p/\sqrt{2\gamma}$ is the betatron frequency and $\Gamma = \dot{\gamma}/\gamma$ is the damping rate due to

relativistic mass increase. Because, in the absence of the laser, $\dot{\gamma} \approx -eE_{\parallel}/mc$, we find that $\Gamma < 0$ for the decelerating electric field, resulting in the growth of betatron oscillations.

To investigate the effect of combining the decelerating longitudinal field with that of a laser, we have propagated an ensemble of test electrons from $x = 0$ to $x = 10^5 \lambda_L$ according to Eqs. (1) and (2). The test electrons were initialized with $p_x = 25mc$ and uniformly loaded into a transverse phase space corresponding to $0 < \varepsilon_{\perp 0} < 1.6mc^2$ as shown in Fig. 1, where particles are color-coded according to gained energy. Note that the maximum of the transverse energy $1.6mc^2$ corresponds to the following ranges of the transverse coordinate and momentum: $|y| < 2.5k_p^{-1}$ and $|p_y| < 9mc$. The simulation parameters $a_0 \equiv eE_0/m\omega_L c = 2.12$, $a_{\parallel} \equiv eE_{\parallel}/m\omega_L c = 0.01$, and $\omega_p = \omega_L/30$ correspond to the laser intensity $I_L = 10^{19} \text{W/cm}^2$, the decelerating field of 0.4 GeV/cm , and the electron plasma density $n = 2 \times 10^{18} \text{ cm}^{-3}$ for the laser wavelength $\lambda_L = 0.8 \mu\text{m}$.

The electron phase space undergoes a complicated fragmentation shown in Figs. 1(a) and 1(b), where four distinct color-coded groups of electrons can be identified. The backward-moving group of particles with the final momentum $p_x \equiv -p_{\text{fin}} \sim -6 \times 10^3 mc$ group (green) corresponds to scenario (2), while the other three groups with $p_x \sim p_{\text{fin}}$ that are color-coded according to their increasing ε_{\perp} as blue, red, and black correspond to scenario (1). Because the work done by the longitudinal force on the forward-moving particles is negative and equal to $\Delta A_W \approx -cp_{\text{fin}}$, by implication, the work done directly by the laser via the inverse ICL mechanism is $\Delta A_L = -2\Delta A_W$. Note that even though $E_{\parallel} \ll E_0$, the

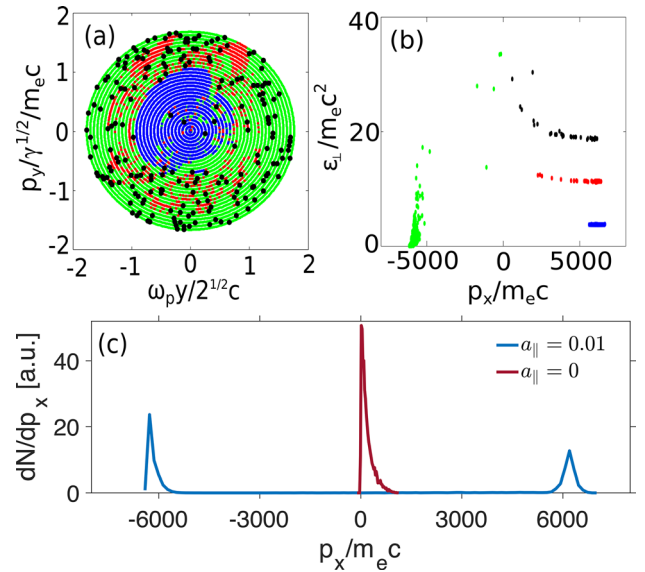


FIG. 1. Inverse ICL acceleration of test electrons in an ion channel by the combination of a laser pulse propagating with the speed of light and a uniform decelerating electric field. (a) Color-coded energy gain as a function of initial conditions in the transverse (y, p_y) phase plane. (b) Four distinct groups of accelerated electrons in the $(p_x, \varepsilon_{\perp})$ phase space: backward-accelerated electrons (green, no laser contribution); forward-accelerated electrons by the laser pulse resonant with the first (blue), third (red), and fifth (black) harmonics of the betatron motion. (c) Electron spectrum with $a_{\parallel} = 0.01$ (blue: all resonant orders) and with $a_{\parallel} = 0$. Propagation distance: $x = 10^5 \lambda_L$. Parameters: $a_0 \equiv eE_0/m\omega_L c = 2.12$, $a_{\parallel} \equiv eE_{\parallel}/m\omega_L c = 0.01$, and $\omega_p = \omega_L/30$.

longitudinal field has a profound stabilizing effect on the inverse ICL acceleration. Remarkably, numerical integration of Eqs. (1) and (2) with $E_{\parallel} = 0$ and other same conditions yields a much smaller maximum achievable electron momentum $p_x \sim 1.2 \times 10^3 mc$. The spectra of electrons with and without a decelerating electric field are compared in Fig. 1(c).

III. ANALYTICAL THEORY

To understand the physics and the limits of the inverse ICL acceleration in the presence of the decelerating electric field, we develop below an analytic theory that assumes (i) linear laser polarization, (ii) luminal phase velocity $v_{\text{ph}} = c$, and (iii) ultra-relativistic forward-accelerated electrons with $p_x \gg mc$. The super-luminal case ($v_{\text{ph}} > c$) is briefly analyzed towards the end of this section and the case of finite ellipticity of the laser field is addressed in Appendix A. For convenience, we replace the longitudinal degrees of freedom (x, p_x) by $(\varphi, \tilde{p}_x \equiv p_x/mc)$ and use the energy-angle variables $I(t) \equiv \varepsilon_{\perp}/mc^2$ and the betatron oscillation phase ψ to express the betatron oscillation as $y = 2(c/\omega_p)\sqrt{I} \cos \psi$, where $\dot{\psi} = \omega_{\beta}$, and we have assumed that in the ultra-relativistic paraxial limit $\gamma \approx \tilde{p}_x$. Assuming that the variation of \tilde{p}_x during one betatron period is small (i.e., $\langle \dot{\psi} \rangle \equiv \langle \omega_{\beta} \rangle \approx \omega_{\beta}$, where $\langle \cdot \rangle$ denotes averaging over one betatron period), the transverse velocity is given by $v_y = v_* \sin \psi$, where $v_*/c = \sqrt{2I/\tilde{p}_x}$.

Next, we introduce the time-averaged equation of motion by averaging the Doppler-shifted laser frequency in the electron's reference frame defined as $\dot{\varphi} = -\omega_D$, where $\omega_D = \omega_L(1 - v_x/v_{\text{ph}}) \approx \omega_L(v_*^2/2c^2) \sin^2 \psi$ for $v_{\text{ph}} = c$. In the paraxial approximation, the time-averaging of $\langle \dot{\varphi} \rangle \equiv -\bar{\omega}_D$ yields $\bar{\omega}_D = \omega_L I / (2\tilde{p}_x)$. Neglecting the difference between $\langle \tilde{p}_x \rangle$ and \tilde{p}_x , the time-averaging of Eq. (1) yields $\dot{\tilde{p}}_x = -\omega_L a_{\parallel} - \omega_L a_0 (v_*/c) \eta$. The time-averaged laser-particle interaction strength $\eta = \langle \sin \psi \cos \varphi \rangle$ does not vanish upon averaging only if the resonance condition $\bar{\omega}_D \approx l\omega_{\beta}$ is satisfied for at least one odd betatron harmonic, in which case $\eta \approx \alpha_l \sin \theta_l$, where $\theta_l = \langle \varphi \rangle + l\psi$ is the phase detuning between the laser field and the odd-integer l 'th harmonic of the betatron motion.^{19,20} The largest non-vanishing coefficients are $\alpha_1 \approx 0.35$, $\alpha_3 = 0.16$, and $\alpha_5 = 0.11$. Note that this resonant condition holds for approximately 40% of electrons in single particle simulations presented in Sec. II.

To further simplify the calculation, we assume the resonance with the l 'th betatron harmonic and express the averaged equations of motion as

$$\dot{\tilde{p}}_x = -\omega_L a_{\parallel} \left(1 + \frac{2v_*}{v_{\text{cr}}^{(l)}} \sin \theta_l \right), \quad \dot{\theta}_l = l\omega_{\beta} - \bar{\omega}_D, \quad (5)$$

$$\dot{I} = I \frac{a_{\parallel} \omega_L}{2\tilde{p}_x}, \quad \dot{\psi} = \omega_{\beta}, \quad \omega_{\beta} = \omega_p / \sqrt{2\tilde{p}_x}, \quad (6)$$

where Eq. (4) was used to express \dot{I} and $v_{\text{cr}}^{(l)} = 2ca_{\parallel}/\alpha_l a_0$ is the critical betatron velocity such that, as shown below, the inverse ICL acceleration stops for $v_* < v_{\text{cr}}^{(l)}$. For a resonant electron with the $(\tilde{p}_x, I) = (p_r, I_r)$ momentum/energy satisfying $\bar{\omega}_D(\tilde{p}_r, I_r) = l\omega_{\beta}(\tilde{p}_r)$, the following relationship must

hold all times: $I_r/\sqrt{2p_r} = l\omega_p/\omega_L$. Therefore, after integrating Eq. (6), we obtain the following solution:

$$\tilde{p}_r(t) = \tilde{p}_0 + a_{\parallel} \omega_L t, \quad \frac{v_r}{c} = \left(\frac{l\omega_p}{\omega_L} \right)^{1/2} \left(\frac{2}{p_r(t)} \right)^{1/4}, \quad (7)$$

where the slow decrease in the resonant electron's transverse velocity $v_r \equiv v_*(I_r, p_r)$ is compensated by the slow drift of its phase according to $\sin \theta_r^{(l)} = -v_{\text{cr}}^{(l)}/v_r(t)$ to ensure the constant-gradient acceleration represented by Eq. (7).

It immediately follows from Eq. (7) that a resonant particle gains energy via the inverse ICL mechanism at the rate that is twice the rate of energy loss to the decelerating longitudinal field regardless of the order of the betatron resonance, i.e., $\Delta A^{(L)} = -2\Delta A^{(W)}$ for any value of $l \geq 1$. However, the resulting transverse energy gains $\varepsilon_{\perp} \propto l$. This scaling explains the physical reason for the fragmentation of the electron phase space observed in Fig. 1(b): the transverse energy "plateaus" of accelerated electrons with different values of ε_{\perp} correspond to different resonant betatron harmonics. Moreover, it follows from $|\sin \theta_r^{(l)}| \leq 1$ that the maximum energy gain corresponding to $\sin \theta_r^{(l)} = -1$ depends on the harmonic number

$$\tilde{p}_{\text{max}}^{(l)} = \frac{l^2 \alpha_l^4}{2} \left(\frac{\omega_p}{\omega_L} \right)^2 \left(\frac{E_0}{E_{\parallel}} \right)^4. \quad (8)$$

Because the quantity $l^2 \alpha_l^4$ decreases with l , the following hierarchy of energy gains is established between the three lowest harmonics: $\tilde{p}_{\text{max}}^{(1)} > \tilde{p}_{\text{max}}^{(3)} > \tilde{p}_{\text{max}}^{(5)}$.

To verify these analytic predictions, three test particles labeled as blue ($l=1$), red ($l=3$), and black ($l=5$) are selected from the phase space shown in Fig. 1(a) and propagated up to $x = 4 \times 10^5 \lambda_L$ (i.e., over a 4 times longer distance than in Fig. 1). The electrons from all three groups are clearly accelerated at the same constant rate as shown in Fig. 2(a). The main distinction between the three groups is their gained transverse energy: $d\varepsilon_{\perp}/dt$ increases with the harmonic number as shown in Fig. 2(b). The amplitude v_* of the betatron velocity, which is extracted from $v_y(t)$ by time-averaging, is shown in Fig. 2(c). As predicted by Eq. (7), v_* decreases with time and the accelerating gradient is kept up at its constant value by the increase in $|\sin \theta|$ as shown in Fig. 2(d). However, when $v_* = v_{\text{cr}}^{(l)}$ and $\sin \theta = -1$ conditions are reached, constant-gradient acceleration stops and the electron's energy starts rapidly decreasing after the critical time $t = t_{\text{max}}$ as shown in Fig. 2(a).

To understand the physics of the abrupt transition at $t = t_{\text{max}}$ from constant-gradient acceleration to rapid deceleration, we linearize Eq. (5) around the resonant particle's momentum according to $\tilde{p}_x = \tilde{p}_r + \delta\tilde{p}$ (here, we assume $l=1$ and drop the harmonic label). A pendulum-like equation is obtained (see Appendix B for the details of the linearization procedure) as follows:

$$\frac{d}{dt} M_I \frac{d\theta}{dt} = -T \left(\frac{v_{\text{cr}}}{v_r(t)} + \sin \theta \right), \quad (9)$$

where $M_I = I^3 \omega_L^2 / \omega_p^4$ and $T = 2\alpha_1 a_0 \omega_p / (I^{1/2} \omega_L)$. Note that $v_r(t) > v_{\text{cr}}$ for early $t < t_{\text{max}}$ times, so that Eq. (9) has a

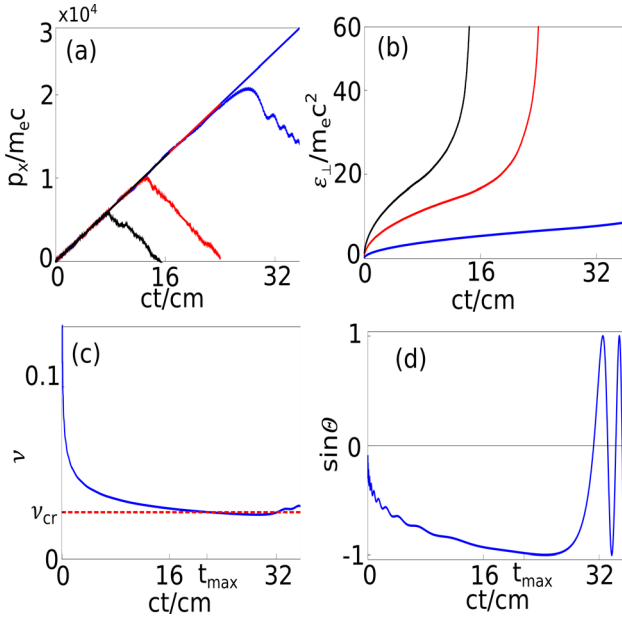


FIG. 2. The dynamics of the representative accelerated electrons from the three groups in Fig. 1 corresponding to the first (blue), third (red), and fifth (black) sub-harmonics of the Doppler-shifted laser frequency ω_D resonantly interacting with electrons' betatron motion in an ion channel: (a) the normalized longitudinal momentum p_x/mc and (b) transverse energy ϵ_{\perp} . (c) Betatron velocity amplitude v_* and (d) phase mismatch θ of the test particle from the first-harmonic resonance group. Constant-gradient acceleration stops when $\sin \theta = -1$ and $v_* = v_{cr}$ [dashed line in (c)]. Parameters: same as in Fig. 1; $\lambda_L = 0.8 \mu\text{m}$.

slowly evolving stable equilibrium point $\theta(t) = -\sin^{-1}(v_{cr}/v_*)$. The equilibrium point disappears at $t = t_{\max}$ when the phase reaches $\theta = -\pi/2$ which separates the oscillation and rotation regions of the pendulum's phase space.

Therefore, for $t > t_{\max}$, the pendulum starts rotating with an increasing speed under the action of a constant torque. In the context of electron acceleration, this implies that, while the amplitude of the Lorentz force is still large because the speed of the betatron oscillations remains close to v_{cr} as shown in Fig. 2(c), the fast oscillations of the mismatch phase θ result in the vanishing of the time-averaged inverse ICL acceleration. This causes electron's overall deceleration by the longitudinal force $-eE_{\parallel}$ as shown in Fig. 2(a) for $t > t_{\max}$.

Note that the phase velocity v_{ph} of the laser wave propagating in the ion channel is slightly higher than the speed of light c despite the low density of the ambient plasma ($\omega_p \ll \omega_L$) and still a lower plasma density inside the channel. Therefore, at least some deviations from the idealized acceleration scaling given by Eq. (7) due to finite $\delta v_{ph} = v_{ph} - c$ is expected. The super-luminal effects are negligible as long as $\delta v_{ph} \ll c - \langle v_x \rangle$ and Eq. (8) holds if $(E_{\parallel}/E_0)^2 \gg \alpha_l^2 \delta v_{ph}/c$ for the l 'th harmonic acceleration. In the opposite limit, maintaining the betatron resonance $-\bar{\omega}_d(p_x, \varphi) + l\omega_{\beta}(p_x) \approx 0$ imposes a slightly modified relationship between transverse energy and longitudinal momentum $I = l\sqrt{2\tilde{p}_x\omega_p/\omega_L} - 3\delta v_{ph}\tilde{p}_x/c$

$$I = l\frac{\omega_p}{\omega_L}\sqrt{2\tilde{p}_x} - 3\delta v_{ph}\tilde{p}_x/c. \quad (10)$$

A modified estimate for the maximum electron energy can be obtained from the condition $dI/d\tilde{p}_x = 0$

$$p_{x,\max}^{(l)} \sim \frac{l^2}{18} \left(\frac{\omega_p}{\omega_L}\right)^2 \frac{1}{(\delta v_{ph}/c)^2}, \quad (11)$$

$$p_{x,\max}^{(5)} > p_{x,\max}^{(3)} > p_{x,\max}^{(1)}. \quad (12)$$

IV. PIC SIMULATIONS

The above simplified model assumes a constant in time decelerating longitudinal field. In reality, such fields cannot be maintained over long distances and time-changing longitudinal fields must be employed. One of the most promising approaches to producing such fields is a laser-wakefield accelerator (LWFA) concept, where significant experimental progress has been recently achieved.^{21–26} Below, we demonstrate that constant-gradient inverse ICL acceleration can be achieved inside a plasma bubble, where externally injected electrons directly interact with the bubble-forming laser pulse and with the decelerating longitudinal field in the front portion of the bubble.

Two-dimensional in space and three-dimensional in electron velocity simulations using a VLPL particle-in-cell (PIC) code²⁷ were carried out for the laser and plasma parameters listed in the caption of Fig. 3. A cold electron bunch injected with the initial momenta $p_{x0} = 25mc$ and $p_{y0} = 0$, the duration $\tau_b = 2\lambda_L/c$, the radius $r_b = 5\lambda_L$, and the density $n_b = 4.3 \times 10^{15} \text{cm}^{-3}$ co-propagates with the laser pump pulse as shown in Fig. 3(a). The front of the bunch initially coincides with the peak of the laser pulse, so that the beam is positioned in the region where the combined effect of the plasma wakefield and of the laser's ponderomotive force is to decelerate the injected electrons. Although the characteristics of the laser pulse and its bubble evolve [see Figs. 3(a) and 3(b) for comparison], the majority of the injected electrons experience a decelerating wakefield throughout the simulation's duration of $t = 700\lambda/c$.

The energy gains from the longitudinal decelerating field, $A_x = -\int eE_x v_x dt$, and from the laser transverse electric field, $A_y = -\int eE_y \cdot v_y dt$, were estimated^{9,15} by extracting $E_{x,y}$ from the PIC simulations and integrating it for each injected electron over a distance of $ct \approx 700\lambda_l = 0.56 \text{mm}$. The results shown in Fig. 3(c) clearly indicate that those electrons that have lost energy to the decelerating field ($A_x < 0$) have gained energy from the laser ($A_y > 0$), and that $A_y \approx -2A_x$ for the highest energy electrons as predicted by the analytic theory. For example, those electrons that have gained $A_y \approx 750mc^2$ from the inverse ICL mechanism have lost $A_x \approx 350mc^2$ to the decelerating electric field, thereby gaining over 200 MeV in energy.

The high-energy electrons roughly correspond to the blue- and red-coded test particles in Fig. 1(b), with some of the electrons undergoing a transition from $l = 1$ to $l = 3$ resonance during the propagation. Their physical location inside the bubble at $x - ct \approx 70\lambda_L$ can be identified in Fig. 3(b) by their large betatron amplitude, and in Fig. 3(d) by their large total energy. On the other hand, the low-energy electrons

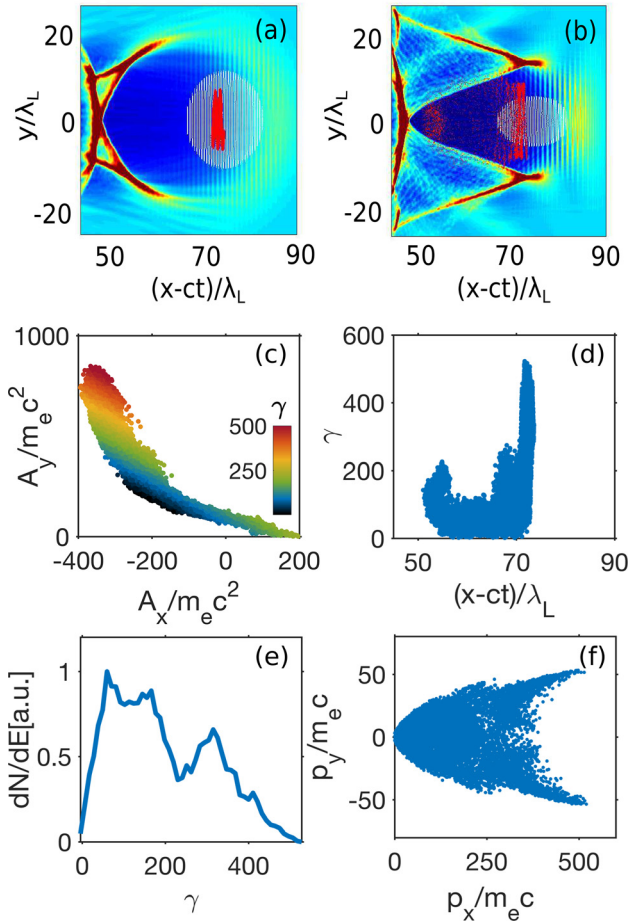


FIG. 3. PIC simulations of inverse ICL acceleration of electrons injected into the decelerating phase of a plasma bubble in a LWFA. Plasma density (color-coded), externally injected electron beam (red dots), and laser intensity contour (white) at (a) $ct = 120\lambda_L$ and (b) $ct = 700\lambda_L$. (c) Electron energy gains from the longitudinal (A_x) and transverse (A_y) electric fields color coded by the relativistic factor γ , (d) the $(x - ct, \gamma)$ phase space, (e) the energy spectrum and (f) the (p_x, p_y) phase space of injected electrons at $ct = 700\lambda_L$. Plasma density $n = 4.3 \times 10^{18} \text{ cm}^{-3}$ and laser parameters: wavelength $\lambda_L = 0.8 \mu\text{m}$, intensity $I = 7.7 \times 10^{19} \text{ W/cm}^2$, pulse duration $\tau = 35 \text{ fs}$, and spot size $w_0 = 12 \mu\text{m}$. Simulation parameters: numerical grid cell size $\Delta x \times \Delta y = \lambda_L/50 \times \lambda_L/5$, four macroparticles per cell.

roughly corresponding to the green-coded test particles in Fig. 1(b) do not directly interact with the laser pulse. Instead, driven by the decelerating wakefield, they initially slip to the back of the bubble at $x - ct \approx 50\lambda_L$, where the wakefield changes sign, and subsequently gain a small amount of energy directly from the wake. Since no energy gain from the inverse ICL mechanism takes place for these electrons, their betatron amplitude is strongly reduced as can be observed in Fig. 3(b). Their physical location inside of the bubble is at $x - ct \approx 55\lambda_L$. As seen from Fig. 3(e), the doubled-peaked spectrum reflects the separation into low- and high-energy electrons. The electrons resonantly interacting with the laser pulse have large transverse and longitudinal momenta, see Fig. 3(f).

V. CONCLUSION

In conclusion, we have proposed a novel approach to constant-gradient far-field particle acceleration: an inverse ion

channel laser combined with longitudinal deceleration. The combination of large transverse momentum and large total energy makes such accelerators promising for developing compact radiation sources. Technological advances in synchronizing electron bunches and laser pulses ensure that the suggested scheme of injecting electrons into a decelerating phase of a plasma bubble will be experimentally realized. Future work will explore the possibility of extending the range of accelerated energies by adiabatically varying plasma parameters.

ACKNOWLEDGMENTS

This work was supported by DOE Grant Nos. DE-SC0007889 and DE-SC0010622, and an AFOSR Grant No. FA9550-14-1-0045. The authors thank the Texas Advanced Computing Center (TACC) at The University of Texas at Austin for providing HPC resources.

APPENDIX A: ACCELERATION BY ELLIPTICALLY POLARIZED LASER WAVE

Similar to the linear polarized wave, an elliptically polarized laser beam also provides constant-gradient direct laser acceleration of electrons in an ion channel whenever an additional *decelerating* longitudinal electric field is introduced. Under the assumption that the laser wave is planar and luminal $E_y^{(L)} = E_1 \cos \phi$, $E_z^{(L)} = E_2 \sin \phi$ and $B_z^{(L)} = E_y^{(L)}$ and $B_y^{(L)} = -E_z^{(L)}$, where $\phi = \omega_L(x/c - t)$, the equations of motion of relativistic electrons now take the following form:

$$\frac{d}{dt} \left(\gamma \frac{dx}{dt} \right) = -\frac{e}{m} E_{\parallel} - \frac{e}{m} \left(\frac{v_y}{c} E_1 \cos \phi + \frac{v_z}{c} E_2 \sin \phi \right), \quad (\text{A1})$$

$$\frac{d}{dt} \left(\gamma \frac{dy}{dt} \right) = -\frac{\omega_p^2 y}{2} + \frac{e E_1}{m} \left(\frac{v_x}{c} - 1 \right) \cos \phi, \quad (\text{A2})$$

$$\frac{d}{dt} \left(\gamma \frac{dz}{dt} \right) = -\frac{\omega_p^2 z}{2} + \frac{e E_2}{m} \left(\frac{v_x}{c} - 1 \right) \sin \phi. \quad (\text{A3})$$

We investigate the interaction of test particles with the elliptically polarized wave considering the case when the ratio between the two orthogonal components of the electric field is equal to 3 ($E_1/E_2 = 3$). The wave intensity, the decelerating electric field and all other parameters are the same as in the case shown in Fig. 1 in Sec. II.

The integration of Eqs. (A1)–(A3) shows that initially homogeneously seeded phase space undergoes strong fragmentation [see Figs. 4(a) and 4(b) for electron phase spaces color-coded in accordance with their final change of the longitudinal momentum] in the same manner as in the case of the linear polarized laser wave shown in Fig. 1. With the exception of green-colored particles that gain negative momentum $p_x < 0$ from the decelerating electric field, all other electrons gain transverse energy ε_{\perp} and positive longitudinal momentum $p_x > 0$ via the DLA mechanism.

In contrast to the linear polarization case, where the electrons were moving mostly in the $(x-y)$ plane, they now move along more complex three-dimensional trajectories.

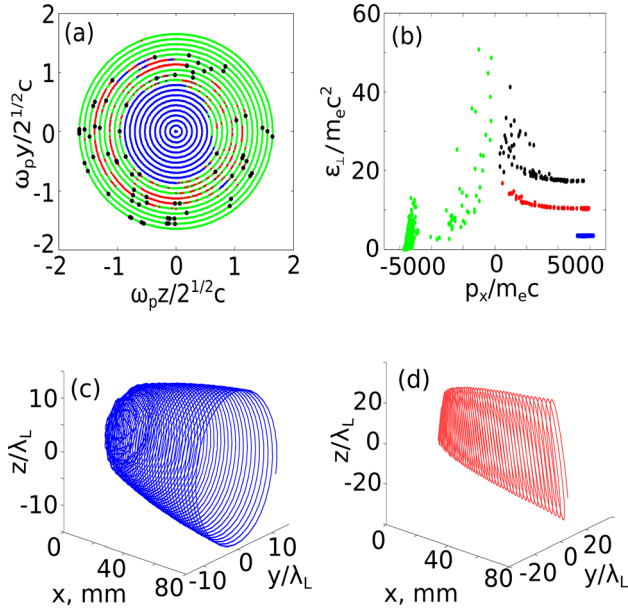


FIG. 4. Acceleration of test electrons in an ion channel by the combination of an elliptically polarized laser pulse ($E_1/E_2=3$) propagating with the speed of light and a uniform decelerating field. (a) Color-coded gain of the longitudinal momentum p_x as a function of the initial conditions in the transverse (y, z) plane. (b) Four distinct groups of accelerated electrons in the (p_x, ϵ_\perp) phase space: backward-accelerated electrons (green, no laser contribution); forward-accelerated electrons by the laser pulse resonant with the first (blue), third (red), and fifth (black) harmonics of the betatron motion. The initial momenta $p_x=25m_e c$ and $p_y=p_z=0$. The other parameters are the same as in the case presented in Fig. 1. Trajectories of the representative electrons accelerated by the first harmonic (c) and the third harmonic (d).

Specifically, the electrons gyrate in the (y - z) plane while propagating in the longitudinal (x -) direction. Our numerical simulations indicate that the exact nature of the electron's gyration depends on the nature of the harmonic order l of the betatron resonance. Here, as in Sec. III, we assume that $\Delta\bar{\omega}_D = l\omega_\beta$, where $\Delta\bar{\omega}_D$ is the time-averaged Doppler shifted laser frequency and ω_β is the betatron frequency.

For example, we find that an electron's trajectory is almost circular in the (y, z) plane if the laser wave is resonant with the first ($l=1$) harmonic of the betatron motion. An example of such trajectory is shown in Fig. 4(c). It is noteworthy that the circular nature of the electron's gyration is preserved, despite the strong ellipticity of the laser pulse. On the other hand, the trajectory can become highly elliptical when the laser wave is resonant with the third ($l=3$) harmonic of the betatron motion. An example of such a trajectory, which is strongly elongated in the z -direction with the axis ratio ~ 9 , is shown in Fig. 4(d). Note that this elongation takes place despite the fact that the laser's polarization ellipse is elongated in the y -direction. The ellipses are squeezed even more for the black-colored ($l=5$) particles.

Note that in the case of circular polarized laser wave ($E_1/E_2=1$), the equation of motion (A1)–(A3) can solve analytically at $l=1$. Electrons move along helical trajectories advancing forward in the x -direction with almost the speed of light and gain maximum energy $\tilde{p}_{\max} \propto (\frac{\omega_p}{\omega_L})^2 (\frac{E_1}{E_0})^4$.

APPENDIX B: SIMILARITY WITH THE MOTION OF PENDULUM

Averaged equations of motion do not depend on time explicitly

$$\dot{\tilde{p}}_x = -\omega_L a_\parallel - \alpha_l \omega_L a_0 (2I/\tilde{p}_x)^{1/2} \sin \theta_l, \quad (\text{B1})$$

$$\dot{\theta} = -\omega_L (I/2\tilde{p}_x) + l\omega_p / (2\tilde{p}_x)^{1/2}, \quad (\text{B2})$$

$$\dot{I} = a_\parallel \omega_L (I/2\tilde{p}_x), \quad (\text{B3})$$

where $I \equiv (I_0 - a_\parallel \phi)$. It is convenient to use the transverse energy I as an independent variable. Dividing Eqs. (B1) and (B2) by Eq. (B3), we obtain for $l=1$

$$\frac{a_\parallel I d\tilde{p}_x}{2\tilde{p}_x dI} = -a_\parallel - \alpha_1 a_0 \left(\frac{2I}{\tilde{p}_x}\right)^{1/2} \sin \theta, \quad (\text{B4})$$

$$-a_\parallel \frac{d\theta}{dI} = 1 - \frac{\omega_p \sqrt{2\tilde{p}_x}}{\omega_L I}. \quad (\text{B5})$$

During steady resonant acceleration $a_\parallel d\theta/dI \ll 1$ and in the zeroth approximation, we obtain from Eqs. (B5) and (B4)

$$\tilde{p}_r = \frac{1}{2} \frac{\omega_L^2}{\omega_p^2} I^2, \quad (\text{B6})$$

$$\sin \theta_r = -\frac{a_\parallel I^{1/2}}{\alpha_1 a_0 (\omega_p/\omega_L)}. \quad (\text{B7})$$

To analyze the solution of Eq. (B1)–(B3) beyond the point where formally $|\sin \theta_r|$ becomes greater than 1, we consider the next approximation by presenting $\tilde{p}_x = \tilde{p}_r + \delta\tilde{p}_x$. Substitution of this expansion into Eqs. (B4) and (B5) yields

$$\frac{a_\parallel I d\delta\tilde{p}_x}{2\tilde{p}_r dI} = [-2a_\parallel - T \sin \theta] \left(1 - \frac{1}{2} \frac{\delta\tilde{p}_x}{\tilde{p}_r}\right), \quad (\text{B8})$$

$$-a_\parallel \frac{d\theta}{dI} = -\frac{1}{2} \frac{\delta\tilde{p}_x}{\tilde{p}_r}, \quad (\text{B9})$$

where $T \equiv 2\alpha_1 a_0 (\omega_p/\omega_L) I^{-1/2}$. Since the expression into square brackets in the r.h.s. of Eq. (B8) is small near the zeroth approximation, we can replace the factor $(1 - \delta\tilde{p}_x/\tilde{p}_r)$ by 1. Then, combining Eqs. (B8) and (B9), we obtain

$$a_\parallel^2 \frac{1}{I} \frac{d}{dI} I^3 \left(\frac{1}{I} \frac{d\theta}{dI}\right) = -2a_\parallel - T \sin \theta. \quad (\text{B10})$$

Introducing new “time” \tilde{t} by formula: $IdI = (\omega_p/\omega_L)^2 d\tilde{p}_r = a_\parallel (\omega_p/\omega_L)^2 \omega_L d\tilde{t}$, we can transform Eq. (B10) into the form

$$\frac{\omega_L^2}{\omega_p^4} \frac{d}{d\tilde{t}} \tilde{p}_r^3 \frac{d\theta}{d\tilde{t}} = -2a_\parallel - T \sin \theta. \quad (\text{B11})$$

Since the difference between \tilde{t} and t is small, we can return to regular time t and obtain Eq. (9).

¹R. B. Palmer, *J. Appl. Phys.* **43**, 3014 (1972).

²Y. Liu, X. J. Wang, D. B. Cline, M. Babzien, J. M. Fang, J. Gallardo, K. Kusche, I. Pogorelsky, J. Skaritka, and A. van Steenbergen, *Phys. Rev. Lett.* **80**, 4418 (1998).

- ³A. van Steenbergen, J. Gallardo, J. Sandweiss, and J.-M. Fang, *Phys. Rev. Lett.* **77**, 2690 (1996).
- ⁴A. A. Kolomenskii and A. N. Lebedev, *Sov. Phys. JETP* **17**, 179 (1963).
- ⁵P. Sprangle, L. Vlahos, and C. M. Tang, "A cyclotron resonance laser accelerator," *IEEE Trans. Nucl. Sci.* **30**, 3177 (1983).
- ⁶R. Shpitalnik, C. Cohen, F. Dothan, and L. Friedland, "Autoresonance microwave accelerator," *J. App. Phys.* **70**, 1101 (1991).
- ⁷D. H. Whittum, A. M. Sessler, and J. M. Dawson, *Phys. Rev. Lett.* **64**, 2511 (1990).
- ⁸A. Pukhov, Z.-M. Sheng, and J. Meyer-ter-Vehn, *Phys. Plasmas* **6**, 2847 (1999).
- ⁹C. Gahn, G. D. Tsakiris, A. Pukhov, J. Meyer-ter-Vehn, G. Pretzler, P. Thirolf, D. Habs, and K. J. Witte, *Phys. Rev. Lett.* **83**, 4772 (1999).
- ¹⁰J. B. Rosenzweig, B. Breizman, T. Katsouleas, and J. J. Su, *Phys. Rev. A* **44**, R6189 (1991).
- ¹¹A. Pukhov and J. Meyer-ter-Vehn, *Appl. Phys. B* **74**, 355 (2002).
- ¹²S. Cipiccia, M. R. Islam, B. Ersfeld, R. P. Shanks, E. Brunetti, G. Vieux, X. Yang, R. C. Issac, S. M. Wiggins, G. H. Welsh *et al.*, *Nat. Phys.* **7**, 867 (2011).
- ¹³I. Nam, M. S. Hur, H. S. Uhm, N. A. M. Hafz, and H. Suk, *Phys. Plasmas* **18**, 043107 (2011).
- ¹⁴J. L. Shaw, F. S. Tsung, N. Vafaei-Najafabadi, K. A. Marsh, N. Lemos, W. B. Mori, and C. Joshi, *Plasma Phys. Controlled Fusion* **56**, 084006 (2014).
- ¹⁵X. Zhang, V. N. Khudik, and G. Shvets, *Phys. Rev. Lett.* **114**, 184801 (2015).
- ¹⁶I. Kostyukov, A. Pukhov, and S. Kiselev, *Phys. Plasmas* **11**, 5256 (2004).
- ¹⁷S. Corde, K. Ta Phuoc, R. Fitour, J. Faure, A. Tafzi, J. P. Goddet, V. Malka, and A. Rousse, *Phys. Rev. Lett.* **107**, 255003 (2011).
- ¹⁸K. Nemeth, B. Shen, Y. Li, H. Shang, R. Crowell, K. C. Harkay, and J. R. Cary, *Phys. Rev. Lett.* **100**, 095002 (2008).
- ¹⁹X. Davoine, F. Fiúza, R. A. Fonseca, W. B. Mori, and L. O. Silva, *J. Plasma Phys.* **84**, 905840304 (2018).
- ²⁰V. Khudik, A. Arefiev, X. Zhang, and G. Shvets, *Phys. Plasmas* **23**, 103108 (2016).
- ²¹J. Faure, Y. Glinec, A. Pukhov, S. Kiselev, S. Gordienko, E. Lefebvre, J. Rousseau, F. Burgy, and V. Malka, *Nature* **431**, 541 (2004).
- ²²C. Geddes, C. Toth, J. Van Tilborg, E. Esarey, C. Schroeder, D. Bruhwiler, C. Nieter, J. Cary, and W. Leemans, *Nature* **431**, 538 (2004).
- ²³S. Mangles, C. Murphy, Z. Najmudin, A. Thomas, J. Collier, A. Dangor, E. Divall, P. Foster, J. Gallacher, C. Hooker *et al.*, *Nature* **431**, 535 (2004).
- ²⁴W. Leemans, B. Nagler, A. Gonsalves, C. Toth, K. Nakamura, C. Geddes, E. Esarey, C. Schroeder, and S. Hooker, *Nat. Phys.* **2**, 696 (2006).
- ²⁵X. Wang, R. Zgadzaj, N. Fazel, Z. Li, S. A. Yi, X. Zhang, W. Henderson, Y. Chang, R. Korzekwa, H. Tsai *et al.*, *Nat. Commun.* **4**, 1988 (2013).
- ²⁶W. P. Leemans, A. Gonsalves, H. S. Mao, K. Nakamura, C. Benedetti, C. B. Schroeder, C. Toth, J. Daniels, D. E. Mittelberger, S. S. Bulanov, J. L. Vay, C. G. R. Geddes, and E. Esarey, *Phys. Rev. Lett.* **113**, 245002 (2014).
- ²⁷A. Pukhov, *J. Plasma Phys.* **61**, 425 (1999).